AGU PUBLICATIONS

JGR

Journal of Geophysical Research: Space Physics

RESEARCH ARTICLE

10.1002/2013JA019738

Key Points:

- Test particle tracing reproduces energetic electron events
- Perpendicular anisotropy dominates further out, parallel anisotropy closer in
- PSBL/lobe source dominates event via reconnection

Correspondence to:
J. Birn,
jbirn@spacescience.org

Citation:
Birn, J., A. Runov, and M. Hesse (2014), Energetic electrons in dipolarization events: Spatial properties and anisotropy, *J. Geophys. Res. Space Physics*, *119*, 3604–3616, doi:10.1002/2013JA019738.

Received 23 DEC 2013
Accepted 8 APR 2014
Accepted article online 3 MAY 2014
Published online 27 MAY 2014

Energetic electrons in dipolarization events: Spatial properties and anisotropy

J. Birn[1,2], **A. Runov**[3], **and M. Hesse**[4]

[1]Space Science Institute, Boulder, Colorado, USA, [2]Guest Scientist, Los Alamos National Laboratory, Los Alamos, New Mexico, USA, [3]Department of Earth, Planetary, and Space Sciences, University of California, Los Angeles, California, USA, [4]NASA Goddard Space Flight Center, Greenbelt, Maryland, USA

Abstract Using the electromagnetic fields of an MHD simulation of magnetotail reconnection, flow bursts, and dipolarization, we further investigate the acceleration of electrons to suprathermal energies. Particular emphasis is on spatial properties and anisotropies as functions of energy and time. The simulation results are compared with Time History of Events and Macroscale Interactions during Substorms observations. The test particle approach successfully reproduces several observed injection features and puts them into a context of spatial maps of the injection region(s): a dominance of perpendicular anisotropies farther down the tail and closer to the equatorial plane, an increasing importance of parallel anisotropy closer to Earth and at higher latitudes, a drop in energy fluxes at energies below ∼10 keV, coinciding with the plasma density drop, together with increases at higher energy, a triple peak structure of flux increases near 0°, 90°, and 180°, and a tendency of flux increases to extend to higher energy closer to Earth and at lower latitudes. We identified the plasma sheet boundary layers and adjacent lobes as a main source region for both increased and decreased energetic electron fluxes, related to the different effects of adiabatic acceleration at high and low energies. The simulated anisotropies tend to exceed the observed ones, particularly for perpendicular fluxes at high energies. The most plausible reason is that the MHD simulation lacks the effects of anisotropy-driven microinstabilities and waves, which would reduce anisotropies.

1. Introduction

Energetic (i.e., suprathermal, tens to hundreds of keV) particle flux increases are a typical signature of dipolarization events in the near magnetotail, associated with substorms [e.g., *Parks and Winckler*, 1968; *Lezniak et al.*, 1968; *Arnoldy and Chan*, 1969; *Baker et al.*, 1978; *Belian et al.*, 1981] and other activity [e.g., *Nakamura et al.*, 2002; *Runov et al.*, 2009; *Sergeev et al.*, 2009; *Deng et al.*, 2010]. These events are characterized by a transient or permanent rapid change from stretched, tail like, to more dipolar magnetic fields. They may consist of an earthward moving brief dipolarization pulse or “dipolarization front,” typically associated with an earthward flow burst [e.g., *Nakamura et al.*, 2002; *Runov et al.*, 2009; *Sergeev et al.*, 2009] or, typically closer to Earth, an increase of B_z toward a more persistent higher level [*Nakamura et al.*, 2009].

The probable cause of the acceleration and energetic particle flux increase is the cross-tail electric field associated with the dipolarization. This conclusion is supported particularly by test particle tracing in assumed or simulated electromagnetic fields of earthward moving electric field pulses associated with localized flow channels [*Birn et al.*, 1997, 1998, 2004; *Li et al.*, 1998; *Zaharia et al.*, 2000; *Ashour-Abdalla et al.*, 2011; *Gabrielse et al.*, 2012; *Pan et al.*, 2014].

Using the three-dimensional time-dependent electric and magnetic field from MHD simulations of near-tail reconnection and flow bursts as basis for test particle studies, we have previously demonstrated major acceleration mechanisms and source regions and provided insights into spatial and temporal variations of electron and ion fluxes [*Birn et al.*, 1997, 2004, 2013]. In the present paper we further investigate electron acceleration and flux properties, extending the results of *Birn et al.* [2013] (Paper 1) on the basis of the same MHD simulation [*Birn et al.*, 2011]. The simulation results are compared to Time History of Events and Macroscale Interactions during Substorms (THEMIS) observations, based on a previously published event with a data selection discussed in section 2. In section 3 we summarize major features of the simulation approach and earlier findings, illustrating typical orbits and source regions of accelerated electrons. Section 4 provides an extended overview of spatial characteristics of injection fronts, while section 5 presents pitch angle dependencies of the electron fluxes and section 6 shows energy dependencies in energy-time spectrograms and energy flux distributions, providing representations closest to empirical results.

2. Observations

In this paper, we use multipoint observations of a dipolarization front observed by THEMIS probes [*Angelopoulos*, 2008] on 27 February 2009 [*Runov et al.*, 2009]. Spectra and energy-time diagrams were taken from two THEMIS probes, THC, located at $x \approx -17\ R_E$, and THD, located at $x \approx -11\ R_E$, between 0750 and 0754 UT. Data from two plasma instruments, the electrostatic analyzer (ESA) [*McFadden et al.*, 2008], which provides ion and electron distribution functions in the 5 eV to 25 keV range with $\Delta E/E \lesssim 20\%$, and the Solid State Telescope (SST) [*Angelopoulos*, 2008], which provides high-energy (30 keV to ~1 MeV) ion and electron fluxes with $\Delta E/E \approx 30\%$, are combined in the spectrograms. Both instruments provide one distribution function per probe spin (~3 s). Magnetic field measurements are provided by the Fluxgate Magnetometer (FGM) [*Auster et al.*, 2008].

3. Simulation Approach and Earlier Findings

In this section we summarize some findings of the earlier investigations [*Birn et al.*, 1997, 2004, 2013], illustrating acceleration mechanisms and source regions. The basis of the investigation are the three-dimensional MHD magnetic and electric fields of a simulation of near-tail reconnection and field collapse [*Birn et al.*, 2011], which were saved at intervals of 1 Alfvén time (800 time steps, corresponding to ~10 s). The simulation included a period of external driving, which lasted until $t = 61$ (in dimensionless time units of ~10 s), causing the formation of a thin embedded sheet of intensified current density in the near tail. After $t = 61$ finite resistivity was imposed, which led to the initiation of reconnection (formation of a neutral line) at $t \approx 90$. However, fast reconnection and the generation of fast flows and strong electric fields did not occur until after $t \approx 125$, when reconnection proceeded to the lobes. The speed up of the evolution apparently was caused by an interaction or reconnection with ballooning-/interchange-type modes, enabled by the entropy reduction in the reconnected lobe magnetic flux tubes [*Birn et al.*, 2011]. In the following, we will refer to the configuration at $t = 61$ as the "initial state."

A realistic conversion of the dimensionless units of the simulation can be based on a magnetic field unit of 12.6 nT, velocity of 1000 km/s, and length unit of ~1.5 R_E, leading to a time unit of 10 s and electric field of 12.6 mV/m. Using these units, the inner boundary of the simulation box corresponds to $x \approx -7.5\ R_E$ and the outer boundary to $x \approx -97.5\ R_E$. In the following, we will mostly use dimensional units but keep the dimensionless times, for better reference to the MHD simulation paper.

Particle orbits were integrated numerically, using linear interpolation of the MHD fields in time. Electron orbits were integrated using a combination of full orbits and gyrodrift orbits, based on the conservation of the magnetic moment μ. The switch between the two types of orbits was based on the magnitude of an adiabaticity parameter, representing the square root of the ratio between field line curvature radius and gyroradius [*Büchner and Zelenyi*, 1989; *Birn et al.*, 2004]. Drift orbit continuity requires a cubic spline interpolation in space. To avoid artificial local maxima and minima, a monotonicity-conserving algorithm was employed [*Hyman*, 1983].

A backward tracing technique [*Curran and Goertz*, 1989] was used to integrate orbits from selected "final" times and locations backward until they reached the initial state or a boundary of the simulation box, using mirroring at the inner boundary. We then applied Liouville's theorem of the conservation of phase space density f along a phase space trajectory to calculate f values and differential energy fluxes at the final destination from the initial and boundary values at the "source" locations. A full distribution function at the chosen final location and time can then be obtained by varying the final energy and pitch angle. Time profiles of fluxes at selected locations, energies, and pitch angles are obtained by varying the times from which particles are launched backward.

Since the MHD simulation does not provide electron information (other than density, which should equal ion density), we must make particular choices in defining the initial and boundary electron distributions at

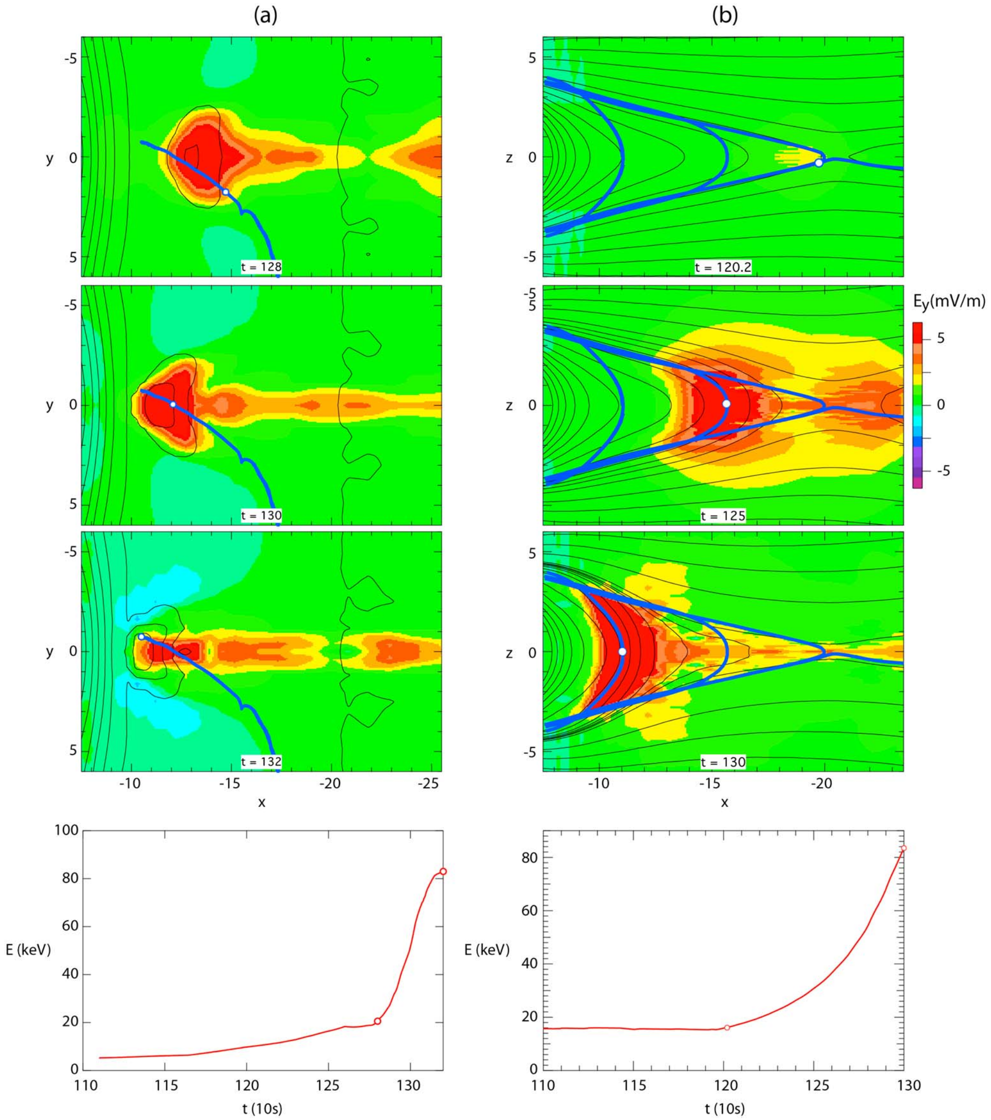

Figure 1. Two different characteristic orbits (heavy blue lines), indicating the two main source regions of accelerated electrons: (a) near-equatorial drift orbit of an electron drifting into the acceleration region from the dusk flank, overlaid on the cross-tail electric field (color) and contours of the magnetic field component B_z (solid black lines), and (b) sections of a bounce orbit projected into the x, z plane, overlaid on the cross-tail electric field (color) and magnetic flux contours (solid black lines). Figures 1a and 1b (bottom) show the electron energies as function of time.

the source locations. For the results reported here, we imposed isotropic kappa distributions [*Vasyliunas*, 1968; *Christon et al.*, 1988, 1989]

$$f(E) \propto \left(1 + \frac{E}{(\kappa - 3/2)kT_e}\right)^{-\kappa-1} \tag{1}$$

with a κ value of 4.5 and chose a fixed initial and boundary temperature $kT_e = 0.3$ keV. These values were largely based on a comparison with the THEMIS results (section 6).

Figures 1a and 1b show two typical electron orbits, illustrating the major acceleration mechanisms as well as the two source regions contributing to enhanced energetic electron fluxes. The colored background shows snapshots of the cross-tail electric field E_y, indicating the earthward propagating flow burst and dipolarization front. Black contours in Figure 1a represent contours of constant B_z shown at intervals of ~6 nT with the contour near $x = -20$ representing the $B_z = 0$ line.

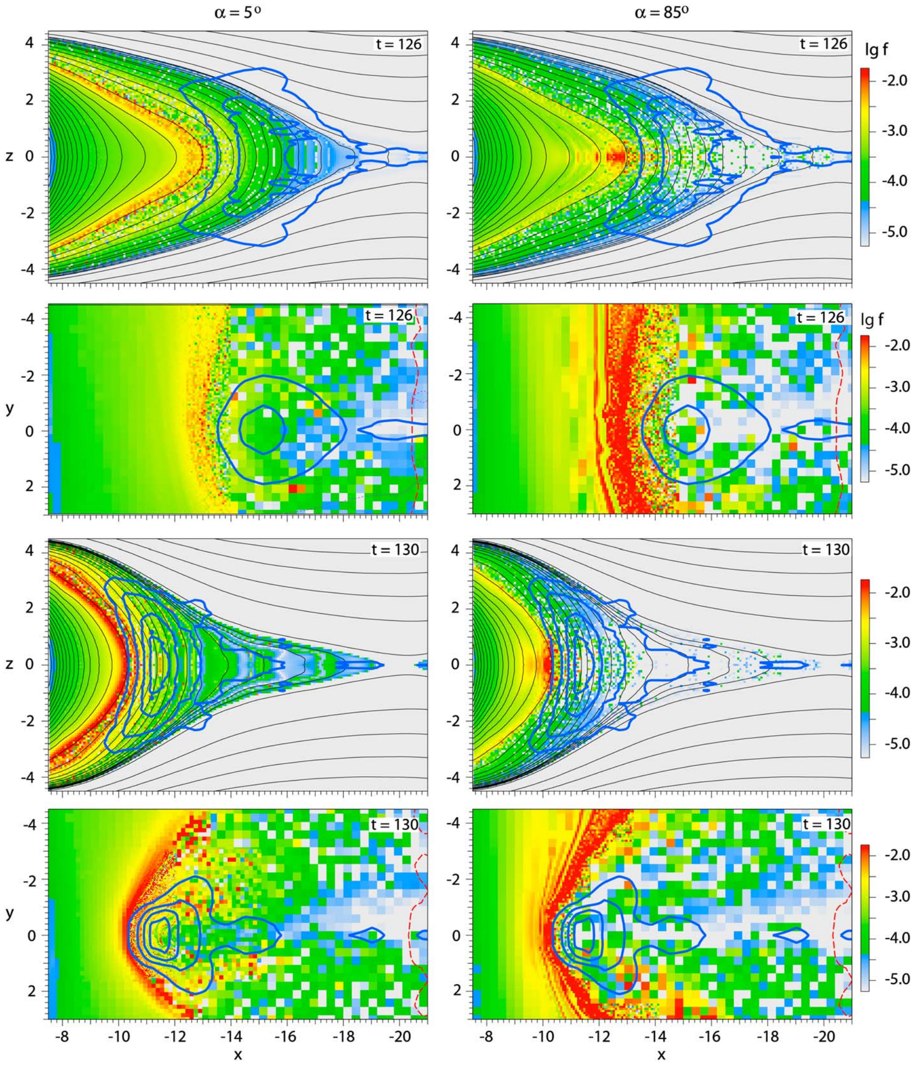

Figure 2. Spatial distribution of 5.2 keV energetic electron fluxes in the x, y and x, z planes for two different pitch angles ($\alpha = 5°$ and $\alpha = 85°$) at two different times, (top) $t = 126$ and (bottom) $t = 130$. The heavy blue contours show the magnitude of the cross-tail electric field at intervals of 1.26 mV/m increasing from 1.26 mV/m (outermost contour). The dashed red lines represent the $B_z = 0$ lines in the x, y plane.

The heavy blue line in Figure 1a represents the near-equatorial orbit of an electron originating from the dusk central plasma sheet, earthward of the reconnection site. The electron drifts into the acceleration region of enhanced cross-tail electric field E_y (color) from the dusk, participates in the earthward collapse, and becomes accelerated primarily by betatron acceleration from the increase in B_z along its orbit. Similar entry and acceleration was found also for low pitch angle orbits that consisted of multiple bounces along a collapsing field line. In that case the energy increase resulted from first-order Fermi acceleration of type B [*Northrop*, 1963], providing a slingshot effect at each equatorial crossing [*Birn et al.*, 2004, 2013].

Figure 1b represents an electron that originally bounces on a closed field line extending into the more distant tail with an apex tailward of the reconnection site. When the field line becomes reconnected, the electron becomes trapped in the inner portion of the field and then participates in the field collapse while bouncing multiple times. (Only three of the bounces are shown in Figure 1b.) We note that during the crossing of the reconnection site the adiabatic assumption breaks down, and the full electron orbit was integrated, including the nonadiabatic effects of the reconnection electric field of the resistive MHD simulation, which is finite at the X-line. In this particular case, however, the electric field at the reconnection site (reconnection rate) was still relatively small so that the direct acceleration was small. The main acceleration in that case then also consisted of first-order Fermi acceleration in the collapsing magnetic field.

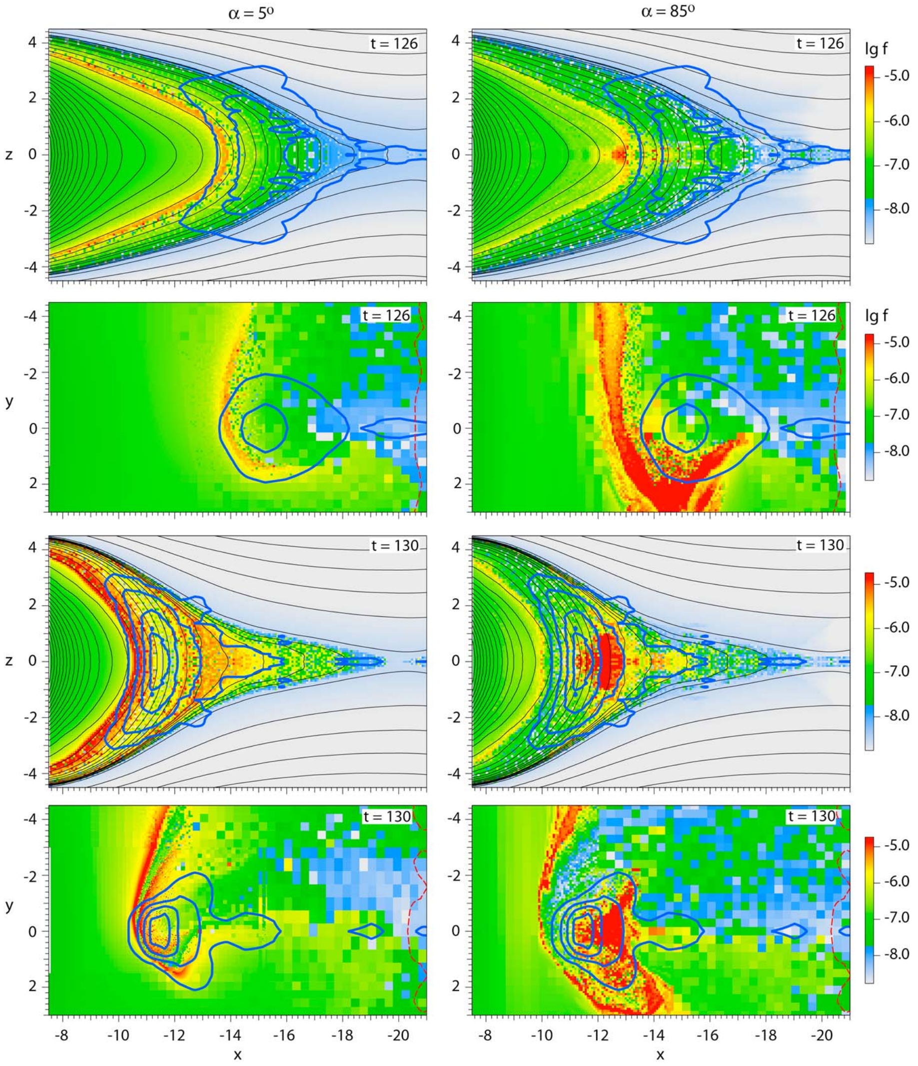

Figure 3. Same as Figure 2 but for 47 keV electron energy.

Generally, the magnetic moment and the pitch angle may change substantially during the full orbit integration when electrons cross the equatorial plane near the reconnection site. Therefore, the final pitch angle is not necessarily uniquely related to the initial pitch angle, and acceleration may involve a combination of different mechanisms, direct acceleration as well as subsequent betatron and Fermi acceleration. Electrons captured at a later time particularly might experience more significant direct acceleration than the one shown in Figure 1b. However, we found that the subsequent Fermi or betatron acceleration still were the dominant mechanisms.

4. Spatial Properties of the Injection Region

An instantaneous picture of the spatial extent of injection regions is hard to obtain from observations without a fleet of spacecraft. The simulations, however, permit us to put local features into the context of large-scale maps. A first, relatively coarse equatorial map of 90°pitch angle, 180 keV proton, and electron fluxes was given by *Birn et al.* [1998], based on test particle tracing in the MHD simulation of *Birn and Hesse* [1996]. Here we present more detailed pictures of the energetic particle flux enhancements in different views.

Figures 2 and 3 show the spatial extent of the injection regions for electrons of 5.2 keV and 47 keV, respectively, for nearly parallel (5° pitch angle) and perpendicular (85° pitch angle) fluxes in the x, y and x, z planes at two different times, $t = 126$ (top) and $t = 130$ (bottom). The black contours show the magnitude of the

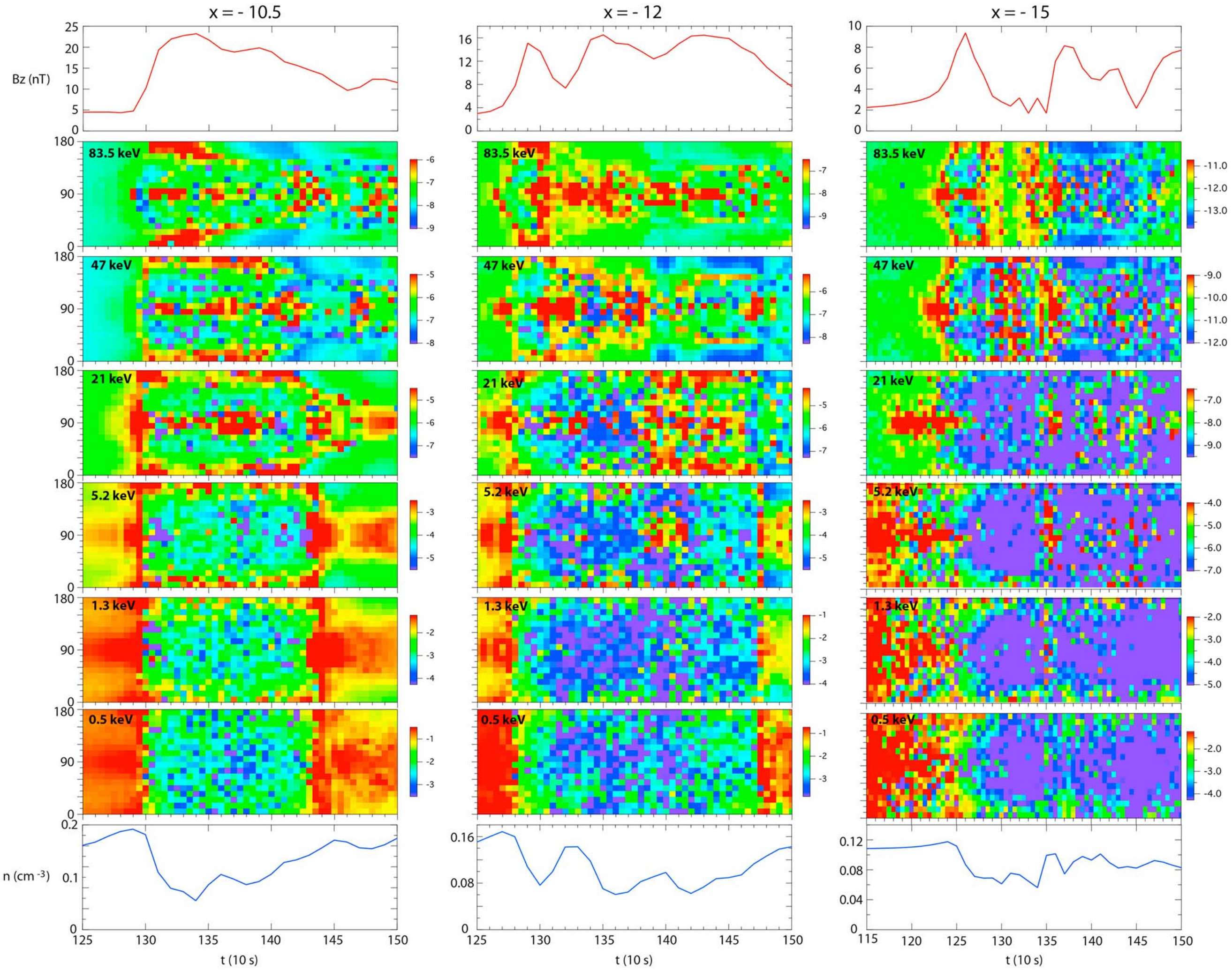

Figure 4. Simulated electron fluxes as functions of time and pitch angle for different energies as indicated at three locations along the *x* axis. (top) The magnetic field B_z and (bottom) the plasma density *n* at the three locations.

cross-tail electric field E_y at intervals of ∼ 3 mV/m. (We note an error in Paper 1: the electric field contours in Figure 7 corresponded to multiples of 2.5 mV/m.) Both figures show that perpendicular energetic electron fluxes are mainly confined to the vicinity of the equatorial plane. Only the low pitch angle fluxes extend to higher latitudes along the field lines, consistent with observed anisotropies [*Runov et al.*, 2013]. At earlier times, farther down the tail, the near-equatorial large pitch angle fluxes clearly dominate, whereas at later times, closer to Earth, the field-aligned fluxes increase in relative magnitude.

At 5.2 keV the equatorial distributions of energetic particle fluxes are quite similar for both pitch angles. However, at 47 keV, the perpendicular flux distribution shows remarkable differences from the parallel fluxes, particularly in their extension toward dusk and even behind the injection front. An inspection of the orbits contributing to these fluxes showed that they result from electrons that drift westward at the inverse B_z gradient associated with the dipolarization front, while losing some of their previously gained energy, after being accelerated in the earthward collapse. This drift may even continue on the westward edge of the front, leading to a deposit of accelerated particles behind the front.

5. Pitch Angle Dependence

The variations of electron fluxes at various energies and locations as functions of time and pitch angle are illustrated in Figure 4, together with the variations of B_z (top) and plasma density (bottom). First, it should be noted that the MHD results (top and bottom) show a density decrease coinciding with the magnetic field increase, as typically observed [*Runov et al.*, 2011]. At low, near thermal, energies, the energetic electron fluxes reflect the behavior of the MHD plasma density, showing a drop when the plasma density is reduced.

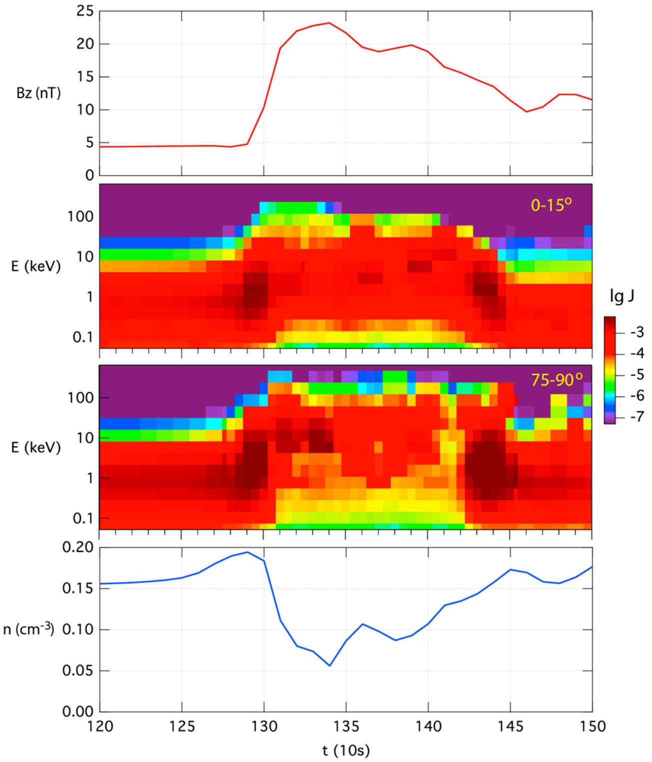

Figure 5. Simulated parallel and perpendicular electron fluxes as functions of time and energy at $x = -10.5$, $y = 0$, $z = 0$. (top) The magnetic field B_z and (bottom) the plasma density n at this location.

At intermediate (5–20 keV) energies, we see a brief enhancement of fluxes just prior to the dipolarization, followed by a drop, except for parallel fluxes around 0° and 180°. At even higher energies (20–80 keV) the fluxes are characterized by a triple peak structure at 0°, 90°, and 180°, observed, for instance, by *Runov et al.* [2012, Figure 10]. A similar structure was also shown by *Wu et al.* [2013, Figure 4], although not commented on. Perpendicular fluxes are more dominant farther down the tail, consistent with observations by *Wu et al.* [2013]. At the most distant location shown, the higher energy electron fluxes around 90° even tend to precede the dipolarization.

6. Energy Dependence

The variations of electron fluxes as functions of time and energy at the location $x = -10.5, y = z = 0$ are illustrated in Figure 5, again together with the variations of B_z (top) and plasma density (bottom). To improve the statistics, the fluxes are averaged over a sliding window of five data points between $t - 0.5$ and $t + 0.5$ (a 10 s window) and six pitch angles in the given range. For comparison, Figure 6 shows parallel and perpendicular differential energy fluxes obtained by THC on 27 February 2009. The shift in the simulated fluxes closely resembles observed characteristics.

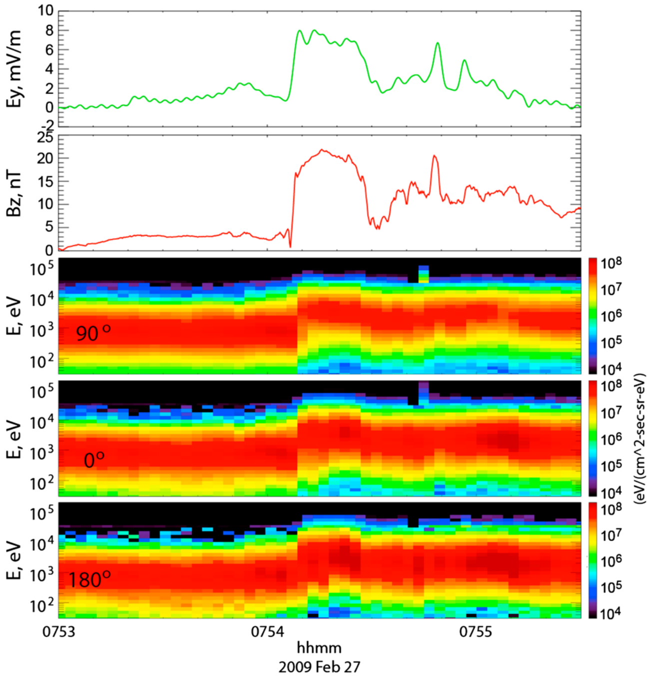

Figure 6. Color-coded parallel and perpendicular differential electron energy fluxes (in eV/s/cm^2/sr/eV) as functions of time and energy obtained by THD at $x \approx -11\ R_E$. The first panel shows the electric field component E_y, and the second panel the magnetic field component B_z.

It is interesting to identify the source regions of the electrons contributing to the change in energy fluxes. Figures 7c and 7d show the source locations in x of the electron orbits at 5° and 85° final pitch angle, contributing to Figure 5, together with B_z from the MHD simulation (Figure 7a) and the omnidirectional distributions of electrons as functions of time and energy (Figure 7b), summed over 18 pitch angles between 0 and 90° and averaged over three adjacent times, separated by 10 s. The flux increases at energies above ∼10 keV reach 2–3 orders of magnitude, consistent with results of *Wu et al.* [2013], although they can vary between different events.

Orange in Figures 7c and 7d indicates electrons with source locations in the inner tail ($x > -22.5$). These particles dominate the distributions before and after the dipolarization event. Since the electric field is very small during these times, they simply follow their gradient/curvature drifts around Earth. Some portion of these electrons thus come from the inner boundary where their drift orbits intersect on the duskside.

It is noteworthy that these origins also dominate during the rise of the fluxes just prior to $t = 130$ (as well as during the decline shortly after $t = 143$), independent of pitch angle and energy. The initial rise in energetic particle fluxes hence is carried by electrons that have drifted from the dusk inner tail plane sheet into the acceleration region, without necessarily encountering the reconnection site.

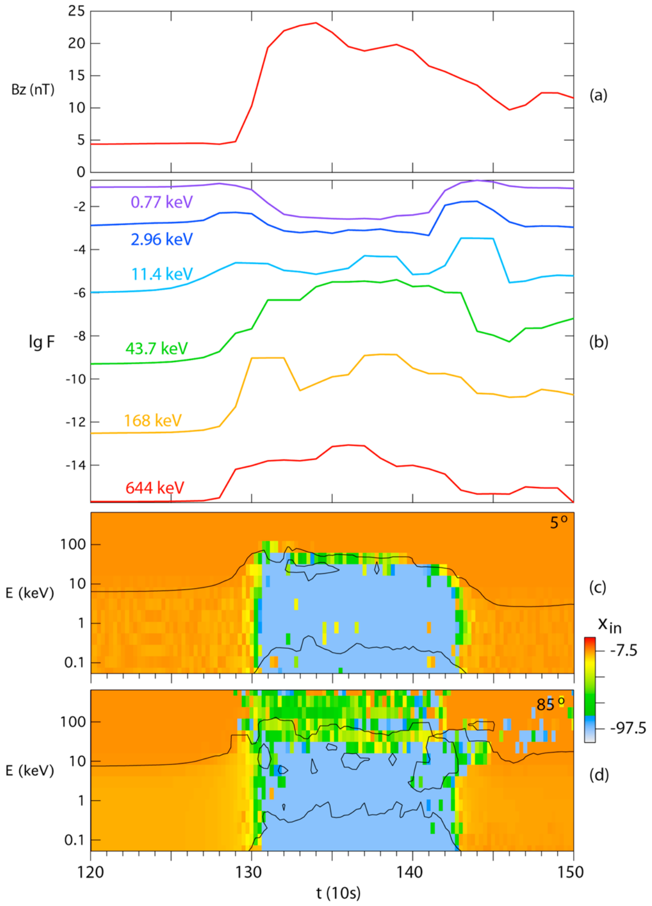

Figure 7. Characteristics of electron fluxes at $x = -10.5, y = z = 0$: (a) magnetic field B_z obtained from the MHD simulation, (b) omnidirectional electron distributions as function of time and energy, (c) origins of electrons contributing to the fluxes shown in Figure 5 for 5° pitch angle, and (d) the same for 85° pitch angle. Black solid lines are contours of lg J, indicating the region of strongest fluxes.

Yellow and green colors indicate origins in the more distant tail ($-92.5 < x < -22.5$). These particles are originally on closed field lines which extend to the more distant tail but become trapped when their field lines undergo reconnection. Blue color indicates origins at the distant boundary. Since we do not consider particle losses or gains at the inner boundary, orbits that are integrated backward across the reconnection site into the plasma sheet boundary or lobe region (PSBL/lobe), where field lines intersect the distant boundary, are reflected at the inner boundary and stopped when they reach the distant boundary. The actual source of these "PSBL/lobe source" electrons might be the ionosphere as well as the plasma mantle converging toward the plasma sheet in the more distant tail. These particles also become trapped in the inner tail when their field lines undergo reconnection.

Because of the short bounce time of the electrons, both distant tail and PSBL/lobe source particles pass the close vicinity of the reconnection site when their field lines undergo reconnection. They hence constitute the reconnection site source considered by *Pan et al.* [2014] in test particle simulations based on a global MHD simulation. Our orbit integration switches to full orbits, conserving the pitch angle, when they approach the reconnection site. The particles hence experience the full nonadiabatic effects of the reconnection electric field in this region. We do not have a full quantitative comparison of the direct acceleration and the subsequent betatron or Fermi acceleration; however, inspection of individual orbits indicates that the direct acceleration is less significant than the subsequent adiabatic acceleration.

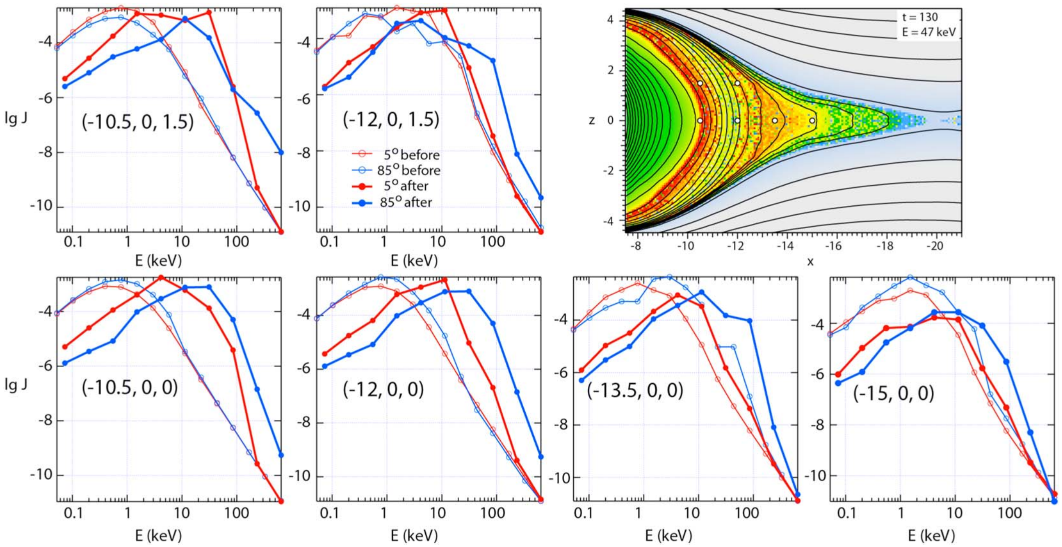

Figure 8. Simulated energy flux distributions before and after the dipolarization at various locations indicated in the panels. The top right panel shows the locations as white dots in the x, z plane superposed on the energy fluxes of 5° pitch angle 47 keV electrons at $t = 130$, as presented in Figure 3.

At energies below ∼100 keV, the main contributions during the shift of the fluxes to higher energies stem from particles originating from the PSBL or the adjacent lobes. This is remarkable because of the low plasma β of 0.01 in the lobes assumed for the MHD simulation. Obviously, this result is very sensitive to the assumed lobe pressure and density. The fact that the shift in energy fluxes appears realistic is an indication that the actual lobe pressure and density are not significantly different than assumed here. These particles contribute to both the flux increases between ∼10 keV and ∼100 keV, and the flux decreases at energies below ∼10 keV, despite the fact that the major portion of the particles below ∼10 keV have also gained substantial amounts of energy. The simple reason for this different behavior is the fact that adiabatic acceleration leads to significant increases in the value of the phase space distribution function in the high-energy power law tail, which overcomes the reduction of the source density in the lobes, whereas at lower energies the latter dominates.

At energies above ∼100 keV, Figures 7c and 7d show a combination of sources in the inner tail, primarily at low pitch angles, and distant tail, particularly at higher pitch angles. The full distributions thus become mixed by various sources.

A more quantitative representation of the spectral changes is provided by Figure 8, showing distributions of parallel and perpendicular differential energy fluxes at various locations before and after the dipolarization. The distributions were averaged over three adjacent energy channels and finite time intervals during which they were found to be reasonably stable. For instance, the before and after intervals for $x = -10.5, y = z = 0$ were taken between $t = 120$ and $t = 126$ before and $t = 131$ and $t = 142$ after (see Figure 5).

For further comparison, we show THEMIS spectra from 27 February 2009 at two similar locations in Figure 9. The simulated fluxes, particularly after the dipolarization, are not as smooth as the observed ones, as they are evaluated for single pitch angles, whereas THEMIS data are integrated over a pitch angle range of ±15° and energy range $\Delta E/E = 0.2$. Nevertheless, one can identify similarities in the typical energy shift and the fact that the maxima of the perpendicular flux increases tend to be larger at larger distance, whereas the peaks of the parallel fluxes dominate closer to Earth (and at higher latitude, consistent with *Runov et al.* [2013]).

Differences between the simulated fluxes and the observed ones are primarily in the perpendicular fluxes at high energies, where the simulated ones exceed the parallel fluxes considerably. A likely reason for this is the absence of kinetic waves and fluctuations in the MHD simulation, which would likely be driven by the simulated anisotropies and cause their reduction.

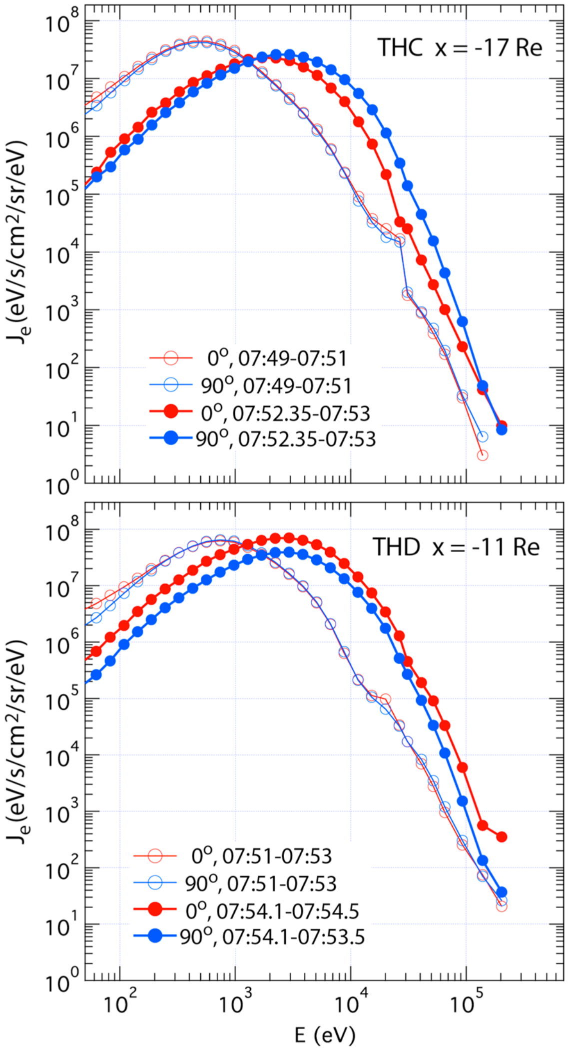

Figure 9. Differential energy flux distributions before and after the dipolarization on 27 February 2009, obtained by THC and THD, located at $x \approx -17\,R_E$ and $x \approx -11\,R_E$, respectively. The fluxes are averaged over the times indicated in the figure.

7. Summary and Discussion

Using a recent MHD simulation of magnetotail reconnection and earthward flow bursts [*Birn et al.*, 2011] as basis for test particle tracing, we extended the investigation of the acceleration of electrons in the electromagnetic fields associated with the rapid dipolarization of an inner magnetotail section and the resulting shift and increase in energy fluxes. Flux estimates were based on backward tracing from the final locations and Liouville mapping from the source regions, assuming isotropic kappa distributions as input. The MHD/test particle approach successfully reproduced several observed injection features and put them into a context of spatial maps of the injection region(s):

(1) Perpendicular anisotropies dominate farther down the tail and closer to the equatorial plane.

(2) Parallel anisotropies become increasingly more important closer to Earth and at higher latitudes. The variation with distance from Earth is consistent with THEMIS observations by *Wu et al.* [2013]. It might also be consistent with observations by *Fu et al.* [2011, 2012], who found an association of perpendicular (“pancake” type) anisotropy with growing dipolarization events (associated with an increase of v_x) and parallel (“cigar” type) anisotropy with decaying events (associated with a decrease in v_x), if one assumes that growing events would be closer to the reconnection site than decaying events. *Fu et al.* [2012], however, did not find such clear spatial association.

Since our imposed distribution functions at the source locations of the electrons are assumed isotropic, anisotropies at the final location can result either from different densities at different source regions or injection times of particles with different pitch angles contributing to a final distribution, or from different histories. Although the sources are distributed in space and time, for most part we did not identify significant differences in the source regions or injection times, such that the history appears to be more important. The anisotropy effects hence indicate that betatron acceleration is more important closer to the reconnection site, where the increase in the magnitude of B_z is more drastic, while Fermi acceleration becomes more important closer to Earth.

(3) Electron fluxes drop at energies below ~10 keV, coinciding with the plasma density drop, while they increase at higher energy above ~10 keV. We identified PSBL/lobe sources, consistent with MHD, for both regions up to about 100 keV. We also found that electrons contributing to the reduction in fluxes at lower energies had gained energy as well as those contributing to the increases at higher energy. The explana-

tion for the difference in the effect is that adiabatic acceleration raises the fluxes more significantly in the high-energy power law tail of the distribution functions, such that it overcompensates the decrease from the reduction in density of the lobe source, whereas the opposite is true at lower energies.

(4) A triple peak structure of flux increases near 0°, 90°, and 180° was found at energies above ∼10 keV. Such structures are observed, for instance, by *Runov et al.* [2012, Figure 10] for energies above ∼10 keV. A similar structure was also shown by *Wu et al.* [2013], although not commented on. Right now, we don't have easy explanation for this result. It seems to indicate that the effects of betatron and Fermi acceleration appear to vary not only as a function of distance from the reconnection site but also tend to be concentrated in phase space around 90° and 0°/180°, respectively. This might be consistent with our finding that the effects also vary with distance from the equatorial plane, such that perpendicular fluxes tend to be spatially localized near the equatorial plane while parallel fluxes extend to high latitudes, causing spatial variations in anisotropies observed as well [*Runov et al.*, 2013].

(5) Flux increases tend to extend to higher energy closer to Earth and at lower latitudes. Since the particle acceleration is a direct consequence of the properties of the electric field in the MHD simulation, these effects apparently are related to the increase of E_y away from the reconnection site, considerably exceeding the reconnection electric field, indicating continued acceleration up to the stopping region of the flow bursts/dipolarization fronts, and to a decrease of the electric field strength away from the equatorial plane.

Our results shed light in particular on the sources of the enhanced (and reduced) energetic particle fluxes, the responsible acceleration mechanisms, and the possible reasons for anisotropies. This supports the view that the localized $\mathbf{v} \times \mathbf{B}$ electric field associated with flow bursts and dipolarization fronts, as obtained in MHD simulations, is indeed the major mechanism affecting particle acceleration as well as causing anisotropies. However, it is also important to note some differences, which might indicate where the MHD/test particle approach needs to be supplemented by additional kinetic effects. Although not obvious from the energy-time and pitch angle-time spectrograms, the energy flux distribution functions show that the simulated anisotropies tend to exceed observed ones. Also, in our modeling, the perpendicular high-energy fluxes tend to extend to higher energies than the parallel fluxes, which is not shown in the observations reported here. Posssible reasons for both are differences in magnetic geometry (resulting in differences between curvature and gradient drifts, affecting the relative importance of Fermi versus betatron acceleration) and the fact that the MHD simulation lacks the presence of kinetic waves, expected to result from anisotropy-driven microinstabilities, which would reduce the anisotropies. Another feature that might play a role is the fact that many observed dipolarization fronts show a strong E_x electric field associated with the kinetic structure of the current layer at the dipolarization front. This might affect energetic particles as well. However, in the present event the E_x component was significantly smaller than E_y at both THC and THD [*Runov et al.*, 2009].

Generally, we note that different observed events may show quite different signatures. For instance, the event presented and modeled by *Pan et al.* [2014] recently seems quite different from the one presented here and earlier by *Runov et al.* [2009], showing a drop in energetic particle fluxes prior to the increase, which is typical also for many injection events observed at geosynchronous orbit. Such differences might be due to differences between different events as well as to differences between different locations within the same event. Despite the fact that *Pan et al.* [2014] modeled a particular event with their global MHD simulation, whereas ours is more generic, several conclusions agree well between our studies. We found that the main source region of energetic particles during the major part of the dipolarization event is the plasma sheet boundary layer or the lobes. Particles from these regions enter the reconnection site and the acceleration region when their field lines become reconnected, as illustrated by Figure 1b. They are hence basically consistent with the reconnection site source assumed and imposed by *Pan et al.* [2014]. Also, the subsequent adiabatic acceleration was identified as the major mechanism for enhancing the energetic particle fluxes in either case.

In addition, we found that the inner plasma sheet source (not included in the *Pan et al.* [2014] study) is the main contribution during the initial rise in the energetic particle fluxes (and the decline at later times) at all energies and pitch angles and at low pitch angles at energies above ∼100 keV. (We should note that the energy thresholds separating different regimes are not to be taken as universal numbers and probably depend on event size and magnitude).

Acknowledgments
The simulation work was performed at Los Alamos under the auspices of the U.S. Department of Energy, supported by NASA grants NNX13AD10G and NNX13AD21G and NSF grant 1203711. THEMIS data analysis was supported by NASA grants NAS5-0299 and NNX13AF81G. We thank V. Angelopoulos for use of data from the THEMIS Mission, C.W. Carlson and J.P. McFadden for use of ESA data, D. Larson and R.P. Lin for use of SST data, D.L. Turner and P. Cruce for help with SST data calibration, and K.-H. Glassmeier, U. Auster, and W. Baumjohann for the use of FGM data provided with financial support through the DLR contract 50 OC 0302. We are grateful to the hospitality and support by the International Space Science Institute Bern, Switzerland, and the fruitful discussions with members of the ISSI working group.

Larry Kepko thanks Rumi Nakamura and an anonymous reviewer for their assistance in evaluating this paper.

References

Angelopoulos, V. (2008), The THEMIS mission, *Space Sci. Rev.*, *141*, 5–34.

Arnoldy, R. L., and K. W. Chan (1969), Particle substorms observed at the geostationary orbit, *J. Geophys. Res.*, *74*, 5019–5028.

Ashour-Abdalla, M., M. El-Alaoui, M. L. Goldstein, M. Zhou, D. Schriver, R. Richard, R. Walker, M. G. Kivelson, and K.-J. Hwang (2011), Observations and simulations of non-local acceleration of electrons in magnetotail magnetic reconnection events, *Nat. Phys.*, *7*, 360–365, doi:10.1038/nphys1903.

Auster, H. U., et al. (2008), The THEMIS fluxgate magnetometer, *Space Sci. Rev.*, *141*, 235–264.

Baker, D. N., P. R. Higbie, E. W. Hones Jr., and R. D. Belian (1978), High-resolution energetic particle measurements at 6.6 R_E: 3. Low-energy electron anisotropies and short-term substorm predictions, *J. Geophys. Res.*, *83*, 4863–4868.

Belian, R. D., D. N. Baker, E. W. Hones Jr., P. R. Higbie, S. J. Bame, and J. R. Asbridge (1981), Timing of energetic proton enhancements relative to magnetospheric substorm activity and its implication for substorm theories, *J. Geophys. Res.*, *86*, 1415–1421.

Birn, J., and M. Hesse (1996), Details of current disruption and diversion in simulations of magnetotail dynamics, *J. Geophys. Res.*, *101*, 15,345–15,358.

Birn, J., M. F. Thomsen, J. E. Borovsky, G. D. Reeves, D. J. McComas, R. D. Belian, and M. Hesse (1997), Substorm ion injections: Geosynchronous observations and test particle orbits in three-dimensional dynamic MHD fields, *J. Geophys. Res.*, *102*, 2325–2341.

Birn, J., M. F. Thomsen, J. E. Borovsky, G. D. Reeves, D. J. McComas, R. D. Belian, and M. Hesse (1998), Substorm electron injections: Geosynchronous observations and test particle simulations, *J. Geophys. Res.*, *103*, 9235–9248.

Birn, J., M. F. Thomsen, and M. Hesse (2004), Electron acceleration in the dynamic magnetotail: Test particle orbits in three-dimensional MHD simulation fields, *Phys. Plasmas*, *11*, 1825, doi:10.1063/1.1704641.

Birn, J., R. Nakamura, E. V. Panov, and M. Hesse (2011), Bursty bulk flows and dipolarization in MHD simulations of magnetotail reconnection, *J. Geophys. Res.*, *116*, A01210, doi:10.1029/2010JA016083.

Birn, J., M. Hesse, R. Nakamura, and S. Zaharia (2013), Particle acceleration in dipolarization events, *J. Geophys. Res. Space Physics*, *118*, 1960–1971, doi:10.1002/jgra.50132.

Büchner, J., and L. M. Zelenyi (1989), Regular and chaotic charged particle motion in magnetotaillike field reversals: 1. Basic theory of trapped motion, *J. Geophys. Res.*, *94*, 11,821–11,842, doi:10.1029/JA094iA09p11821.

Christon, S. P., D. G. Mitchell, D. J. Williams, L. A. Frank, C. Y. Huang, and T. E. Eastman (1988), Energy spectra of plasma sheet ions and electrons from ∼50 eV/e to ∼1 MeV during plasma temperature transitions, *J. Geophys. Res.*, *93*, 2562–2572.

Christon, S. P., D. J. Williams, D. G. Mitchell, L. A. Frank, and C. Y. Huang (1989), Spectral characteristics of plasma sheet ion and electron populations during undisturbed geomagnetic conditions, *J. Geophys. Res.*, *94*, 13,409–13,424.

Curran, D. B., and C. K. Goertz (1989), Particle distributions in a two-dimensional reconnection field geometry, *J. Geophys. Res.*, *94*, 272–286.

Deng, X., M. Ashour-Abdalla, M. Zhou, R. Walker, M. El-Alaoui, V. Angelopoulos, R. E. Ergun, and D. Schriver (2010), Wave and particle characteristics of earthward electron injections associated with dipolarization fronts, *J. Geophys. Res.*, *115*, A09225, doi:10.1029/2009JA015107.

Fu, H. S., Y. V. Khotyaintsev, M. André, and A. Vaivads (2011), Fermi and betatron acceleration of suprathermal electrons behind dipolarization fronts, *Geophys. Res. Lett.*, *38*, L16104, doi:10.1029/2011GL048528.

Fu, H. S., Y. V. Khotyaintsev, A. Vaivads, M. André, V. A. Sergeev, S. Y. Huang, E. A. Kronberg, and P. W. Daly (2012), Pitch angle distribution of suprathermal electrons behind dipolarization fronts: A statistical overview, *J. Geophys. Res.*, *117*, A12221, doi:10.1029/2012JA018141.

Gabrielse, C., V. Angelopoulos, A. Runov, and D. L. Turner (2012), The effects of transient, localized electric fields on equatorial electron acceleration and transport toward the inner magnetosphere, *J. Geophys. Res.*, *117*, A10213, doi:10.1029/2012JA017873.

Hyman, J. M. (1983), Accurate monotonicity preserving cubic interpolation, *SIAM J. Sci. Stat. Comput.*, *4*, 645–654.

Lezniak, T. W., R. L. Arnoldy, G. K. Parks, and J. R. Winckler (1968), Measurement and intensity of energetic electrons at the equator at 6.6 R_E, *Radio Sci.*, *3*, 710–714.

Li, X., D. N. Baker, M. Temerin, G. D. Reeves, and R. D. Belian (1998), Simulation of dispersionless injections and drift echoes of energetic electrons associated with substorms, *Geophys. Res. Lett.*, *25*, 3763–3766.

McFadden, J. P., C. W. Carlson, D. Larson, V. Angelopolos, M. Ludlam, R. Abiad, and B. Elliot (2008), The THEMIS ESA plasma instrument and in-flight calibration, *Space Sci. Rev.*, *141*, 277–302.

Nakamura, R., et al. (2002), Motion of the dipolarization front during a flow burst event observed by Cluster, *Geophys. Res. Lett.*, *29*(20), 1942, doi:10.1029/2002GL015763.

Nakamura, R., A. Retinò, W. Baumjohann, M. Volwerk, N. Erkaev, B. Klecker, E. A. Lucek, I. Dandouras, M. André, and Y. Khotyaintsev (2009), Evolution of dipolarization in the near-Earth current sheet induced by Earthward rapid flux transport, *Ann. Geophys.*, *27*(4), 1743–1754.

Northrop, T. G. (1963), *The Adiabatic Motion of Charged Particles*, Interscience, New York.

Pan, Q., M. Ashour-Abdalla, R. J. Walker, and M. El-Alaoui (2014), Electron energization and transport in the magnetotail during substorms, *J. Geophys. Res. Space Physics*, *119*, 1060–1079, doi:10.1002/2013JA019508.

Parks, G. K., and J. R. Winckler (1968), Acceleration of energetic electrons observed at the synchronous altitude during magnetospheric substorms, *J. Geophys. Res.*, *73*, 5786–5791.

Runov, A., V. Angelopoulos, M. I. Sitnov, V. A. Sergeev, J. Bonnell, J. P. McFadden, D. Larson, K.-H. Glassmeier, and U. Auster (2009), THEMIS observations of an earthward-propagating dipolarization front, *Geophys. Res. Lett.*, *36*, L14106, doi:10.1029/2009GL038980.

Runov, A., V. Angelopoulos, X.-Z. Zhou, X.-J. Zhang, S. Li, F. Plaschke, and J. Bonnell (2011), A THEMIS multicase study of dipolarization fronts in the magnetotail plasma sheet, *J. Geophys. Res.*, *116*, A05216, doi:10.1029/2010JA016316.

Runov, A., V. Angelopoulos, and X.-Z. Zhou (2012), Multipoint observations of dipolarization front formation by magnetotail reconnection, *J. Geophys. Res.*, *117*, A05230, doi:10.1029/2011JA017361.

Runov, A., V. Angelopoulos, C. Gabrielse, X.-Z. Zhou, D. Turner, and F. Plaschke (2013), Electron fluxes and pitch-angle distributions at dipolarization fronts: THEMIS multipoint observations, *J. Geophys. Res. Space Physics*, *118*, 744–755, doi:10.1002/jgra.50121.

Sergeev, V. A., V. Angelopoulos, S. Apatenkov, J. Bonnell, R. Ergun, R. Nakamura, J. McFadden, D. Larson, and A. Runov (2009), Kinetic structure of the sharp injection/dipolarization front in the flow-braking region, *Geophys. Res. Lett.*, *36*, L21105, doi:10.1029/2009GL040658.

Vasyliunas, V. M. (1968), A survey of low-energy electrons in the evening sector of the magnetosphere with OGO 1 and OGO 3, *J. Geophys. Res.*, *73*, 2839–2884.

Wu, M. Y., Q. M. Lu, M. Volwerk, Z. Vörös, T. L. Zhang, L. C. Shan, and C. Huang (2013), A statistical study of electron acceleration behind the dipolarization fronts in the magnetotail, *J. Geophys. Res. Space Physics*, *118*, 4804–4810, doi:10.1002/jgra.50456.

Zaharia, S., C. Z. Cheng, and J. R. Johnson (2000), Particle transport and energization associated with substorms, *J. Geophys. Res.*, *105*, 18,741–18,752.